


High Resolution Optical Coherence Tomography

Xin Ge, Shufen Chen, Si Chen, and Linbo Liu , *Member, IEEE*

(Invited Paper)

Abstract—Imaging cellular and extracellular structures and processes *in situ* and *in vivo* is highly desired for the understanding and diagnosis of human diseases. High resolution optical coherence tomography (HR-OCT) is particularly suitable for this task because it can provide real-time, 3-D images of a large tissue volume at subcellular resolution. Over the past two decades, tremendous technical advances have been made to tackle the fundamental and practical limitations of HR-OCT for applications in various clinical fields. Meanwhile, novel scientific and clinical applications of HR-OCT have also been proposed and validated. This review aims to provide an update on the progress of technology development, with a focus on axial focus extension, aberration correction, and fiber-optic probe development. This review also aims to summarize the newly established capabilities of HR-OCT in fundamental and clinical research, in an effort to promote multidisciplinary research using this powerful imaging tool.

Index Terms—High-resolution imaging, optical coherence tomography.

I. INTRODUCTION

SINCE its first launch in the early 1990s [1], optical coherence tomography (OCT) has been established as a powerful diagnostic imaging tool. OCT provides three-dimensional (3D) imaging of tissue microstructures in a non-contact and non-destructive manner. In addition, it enables functional imaging and measurements such as angiography [2], optometry [3], flow [4], birefringence [5], spectroscopic [6] and mechanical (stress/strain) measurements [7]. While the original form of OCT was successfully used for ophthalmic diagnosis, there have been a number of technical gaps between the clinical needs and the technical parameters, such as speed, penetration depth, spatial resolution and cost. As an optical biopsy tool that fulfills the goal of ‘*in vivo* histology’, OCT is expected

Manuscript received October 16, 2020; revised January 2, 2021; accepted February 20, 2021. Date of publication February 23, 2021; date of current version June 16, 2021. This work was supported in part by the Singapore Ministry of Health’s National Medical Research Council under its Open Fund Individual Research Grant MOH-OFIRG19may-0009, in part by the Ministry of Education Singapore under its Academic Research Fund Tier 1 Grant 2018-T1-001-144, and in part by the Academic Research Funding Tier 2 Grant MOE-T2EP30120-0001. (Corresponding author: Linbo Liu.)

Xin Ge, Shufen Chen, and Si Chen are with the School of Electrical and Electronic Engineering, Nanyang Technological University, Singapore, 639798 (e-mail: ustcgxtc@gmail.com; sophia_chen01@hotmail.com; si.chen@ntu.edu.sg).

Linbo Liu is with the School of Electrical & Electronic Engineering, and also with the School of Chemical & Biomedical Engineering, Nanyang Technological University, Singapore, 639798 (e-mail: liulinbo@ntu.edu.sg).

Color versions of one or more of the figures in this article are available online at <https://doi.org/10.1109/JLT.2021.3061606>.

Digital Object Identifier 10.1109/JLT.2021.3061606

to image subcellular and extracellular structures which play critical roles in pathophysiological processes. Towards this goal, cellular and subcellular resolution imaging technologies have been developed (Fig. 1), particularly since Fourier domain OCT (FD-OCT) is introduced around 2000. The improvements in the axial resolution are attributed to the advancements in the broadband light sources, including femtosecond lasers, multiplexed superluminescent diodes (SLD), and supercontinuum generation sources. While the axial resolution has a simple solution, the improvement in the transverse resolution is complicated by the trade-offs between the transverse spot size and axial focal range, aberrations, and ranging depth. In order to implement high resolution in fiber-optic probe, there are also practical constraints including the diameter and rigid length of the distal end optics, working distance, scanning speed and data size, in addition to the fundamental trade-offs. In this review, we firstly summarize the key parameters of OCT imaging in section II, and then provide an overview of technologies that improve the spatial resolutions and mitigate the above-mentioned trade-offs and constraints, including ultrahigh-resolution OCT (UHR-OCT), Micro-OCT, and methods for axial focus extension and aberration correction in section III. Finally, we demonstrate the potential of high resolution OCT for disease diagnosis and clinical research in the field of ocular imaging and internal organ imaging in Section IV.

Since high resolution is a generic term used in many occasions, it is important to clarify that high resolution in this review refers to cellular or subcellular level resolutions, that is to say, 1–2 μm in tissue. Normally, an ophthalmic OCT system provides a spatial resolution around 10 μm (axial in air) by 15–20 μm (transverse), and an endoscopic or intracoronary OCT system provides a spatial resolution around 10 μm (axial in air) by 30–40 μm (transverse). Therefore, the spatial resolutions of HR-OCT are around one order of magnitude higher than those of the current clinical systems. It is also worth mentioning that full-field approaches, including full-field optical coherence microscopy and full-field optical coherence tomography, which normally capable of achieving 1–2 μm spatial resolution(s) or even higher, are not included in this review unless necessary.

II. SUMMARY OF KEY PARAMETERS IN OCT

Normally, image formation in OCT is the same as low-coherence interference in the axial direction and confocal microscopy in the transverse direction. Light partially reflected or scattered from the sample interferes with a reference wave reflected from the reference mirror, and projected onto a pinhole

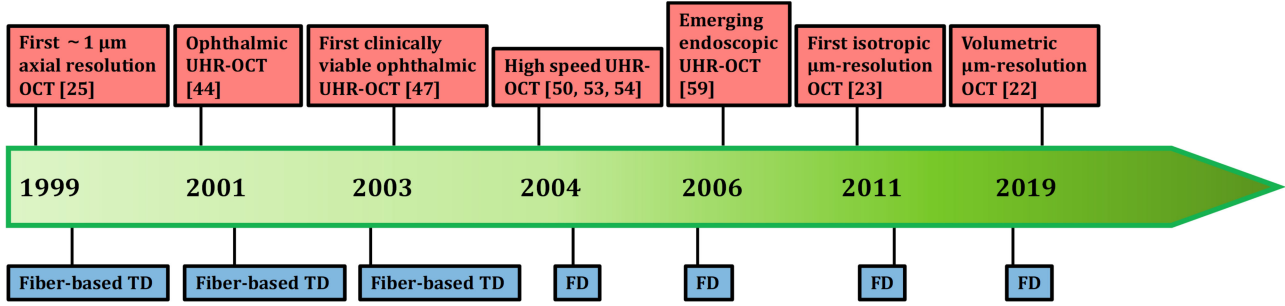


Fig. 1. Timeline illustrating the generation of UHR-OCT system in technical achievement (top) and coherence domain (bottom).

detector. The detected interference signals are post-processed to generate images in real space. Take spectral domain OCT (SD-OCT) for example, the detected interference signal $I(k)$ in k -space, including direct-current (DC) term, cross-correlation (CC) term, and auto-correlation (AC) term, can be denoted as the following formulation,

$$I(k) = S(k)[DC + 2 \int_{-\infty}^{\infty} \sqrt{I_r(k)I_s(k)} \cos(2kz) dz + AC] \quad (1)$$

where $S(k)$ is the spectral distribution of the light source. $I_r(k)$ and $I_s(k)$ are the squared magnitude of the electric field reflectivity from the reference arm and the sample arm at the depth of z . Resolutions, lateral field of view, axial field of view or focal range, sensitivity and ranging depth are the most important parameters used to evaluate an OCT system.

Different from the conventional microscopy, the axial resolution Δz or the optical “sectioning” capability of OCT is depended on the coherence length of the light source and decoupled from the transverse resolution Δx . The axial resolution is proportional to the square of the central wavelength λ_0 and is inversely proportional to the bandwidth of the light source $\Delta \lambda$. Assuming a Gaussian power spectrum, the axial resolution is denoted as,

$$\Delta z = \frac{2 \ln 2 \lambda_0^2}{\pi \Delta \lambda} \quad (2)$$

Transverse resolution Δx is no difference with the conventional microscopy, which is inversely proportional to the spot size at the lens pupil d and is proportional to the focal length f ,

$$\Delta x = \frac{4\lambda f}{\pi d} \quad (3)$$

Lateral field of view is related to a maximum one-sided scan angle θ_{\max} , can be given by:

$$FOV_{\text{lateral}} = 2f\theta_{\max} \quad (4)$$

The transverse resolution Δx is also linked to the depth of field or the confocal parameter b , which is defined as the axial range where beam radius is increased by a factor of $\sqrt{2}$ with respect to the beam waist:

$$b = \frac{\pi \Delta x^2}{\lambda} \quad (5)$$

It should be noted that the confocal parameter above is derived under the assumption of a Gaussian beam, and does not apply

for non-Gaussian beams such as Bessel beams [8] or airy beams [9]. In the context of OCT imaging, since the dynamic range of OCT signal is normally more than 100 dB and the images are normally presented in log scale, the high quality axial image range is always larger than the depth of focus. More often, axial field of view or axial focal range is used, which is defined as the full-width-at-half-maximum (FWHM) range of the confocal axial response function [10]:

$$FOV_{\text{axial}} = \frac{0.221 \cdot \lambda}{\sin^2 \left[\frac{\sin^{-1} NA}{2} \right]} \quad (6)$$

where NA is the numerical aperture of focusing system defined as $NA = \sin(\alpha)$, and α is half the angular optical aperture subtended by the objective at the intensity level of $1/e^2$.

The theoretical sensitivity can be calculated as [11],

$$S [dB] = 10 \log_{10} \left(\frac{N_{ref} \times \sum N_S}{N_{sh}^2 + N_{el}^2 + N_{RIN}^2} \right) \quad (7)$$

where N_{ref} is the number of electrons in pixel by reference arm, N_S is the sum of electrons over the entire array by sample arm, N_{sh} is the number of shot noise electrons, N_{el} is the electrical noise of the detector and N_{rin} is the RIN noise. Detailed comparison on the signal to noise ratio (SNR) for time domain OCT (TD-OCT), swept source OCT (SS-OCT) and Fourier domain (FD-OCT) can be found in ref. [12] and [13]. Theoretically, FDOCT systems have a sensitivity of >20 dB more than TDOCT systems [10]. Sensitivity is a key feature of OCT system. Normally, a weakly reflective structures with a reflectivity R as low as 10^{-10} can be detected by a state-of-the-art FD-OCT.

Optimal sensitivity requires optimal efficiency of all the components and sub-systems in an OCT setup. In addition to efficiency, sensitivity also suffers from the ‘roll-off’ effect due to the nonlinear-wavenumber sampling and the undersampling of interference fringes in FD-OCT. Assuming the sampling is linear in wavenumber, 6-dB fall-off depth is [10]:

$$z_{6dB} = \frac{\ln 2}{\delta_r k} \quad (8)$$

Here $\delta_r k$ is the FWHM spectral resolution in wavenumber. Limited by the Nyquist sampling theorem, maximum imaging depth can be calculated as [10], [14]:

$$z_{\max} = \frac{\pi}{2\delta_s k} \quad (9)$$

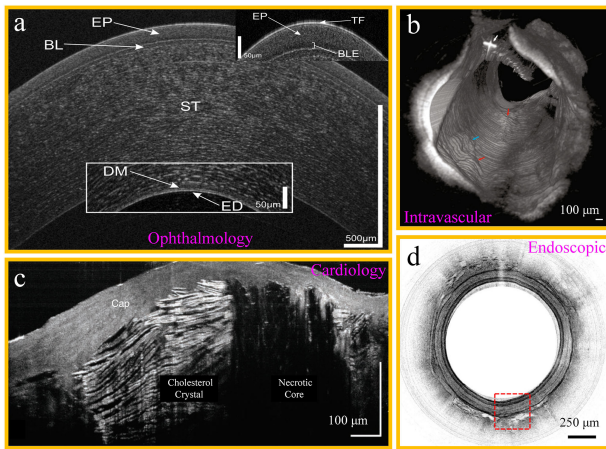


Fig. 2. UHR-OCT and μ OCT in ophthalmology, cardiology, intravascular and endoscopic trials (a) A representative cross-sectional image of a healthy human cornea, TF, tear film; EP, epithelium; BLE, basal layer of epithelium; BL, Bowman's layer; ST, corneal stroma; DM, Descemet's membrane; ED, endothelium. This figure is adopted from reference [21]. (b) 3D reconstruction of atherosclerotic rabbit aorta. The white arrow indicates the guide wire. The blue and red arrows indicate atherosclerotic plaque regions. This figure is adopted from reference [22]. (c) Cholesterol crystals in atheromatous plaques detail as linear, highly reflecting structures within a necrotic core. This figure is adopted from reference [23]. (d) A representative circumferential image of rat esophagus *in vivo*. This figure is adopted from reference [24].

Here $\delta_s k$ is the spectral sampling interval in wavenumber. More detailed model and analysis of sensitivity roll-off can be found in [13], [15].

III. RESOLUTION IMPROVEMENT IN OCT

HR-OCT enables detailed visualization of the microscopic structures in various tissue systems (Fig. 2) *ex vivo* and *in vivo*. A list of representative efforts is provided in Table I. Most of HR-OCT systems employ light sources with a centered wavelength of ~ 800 nm and spectral bandwidth of >200 nm. This is because of a favored penetration depth and relative higher transverse and axial resolutions. As shown in (2), the transverse and axial resolutions have linear and quadratic dependence on the center wavelength. Therefore, the shorter the wavelength is, the higher the resolutions are. Achieving cellular-level axial resolution (~ 2 μ m in air) at 1000 nm or 1300 nm requires a FWHM spectral bandwidth of around 300 nm and 500 nm [16], respectively, which is much more difficult than at 800 nm. One of other benefits of imaging in the 800 nm wavelength range is better imaging contrast because of higher scattering coefficient of biological tissue and weaker absorption by water at 800 nm than at 1300 nm (O-band). Recently, visible-light OCT has emerged as a promising approach [17]–[20]. Compared with imaging in the 800 nm wavelength range, visible range can provide higher resolutions and specific spectroscopic contrast at the expense of penetration depth, sensitivity, and imaging speed.

There are also a number of drawbacks of imaging in the 800 nm wavelength range and with a large spectral bandwidth. Firstly, the penetration depth is much shorter than that of longer wavelength sources due to higher scattering coefficient of biological tissues. Secondly, the insertion loss of fiber optic components, such as coupler and circulator, at 800 nm is

significantly higher than those in the O-band, resulting in lower OCT sensitivity. Thirdly, Si-based linear array detectors' quantum efficiency is suboptimal in the longer wavelength side of the spectrum centered at 800 nm, which also affects the sensitivity. Fourthly, the component cost is mainly dependent on the market size in the telecommunication applications. Therefore, most of the components, except for the light source and the detector, are more costly in the 800 nm region than in the O-band.

The specific microscopic information uncovered by different imaging systems may be very different, depending on the light source (center wavelength, bandwidth, spectral shape, and noise performances), sample arm optics (transverse resolution and aberration management), interferometer efficiency, detector efficiency and speed.

A. Ultrahigh-Resolution OCT (UHR-OCT)

Since the axial resolution is decoupled with the transverse resolution, it is possible to achieve an ultrahigh axial resolution (1–3 μ m) with the standard transverse resolution (~ 10 –30 μ m) with the advent of ultra-broad bandwidth light sources. Light sources for UHR-OCT are often classified into four types: femtosecond lasers, supercontinuum (SC) sources, SLDs and swept sources (SS).

B. Micro-OCT (μ OCT)

UHR-OCT satisfies the need for imaging layered structures such as retinal layers. In order to resolve cellular and extracellular structures in 2D (tomography) and 3D, a new class of technology termed, Micro-OCT (μ OCT) has been developed that provides 1–2 μ m spatial resolutions in both axial and transverse directions. μ OCT typically employs SC sources for achieving axial resolution of ~ 1 - μ m in tissue. The major technical challenges with μ OCT are limited axial focal range, aberrations with the sample arm optics and caused by the sample.

C. Axial Focus Extension Techniques

The diffraction limited depth of field of a Gaussian beam corresponding to a ~ 2 –3 μ m transverse resolution is typically 30–70 μ m at 800 nm, and the corresponding axial field of view is around 100–200 μ m [25], [26]. In order to image the out-of-focus regions, the simplest way is C-mode imaging, where sample zones along depth are scanned sequentially by mechanically shift the sample and images of all the zones are fused together to render an extended axial field of view [25]. In order to bring OCT resolutions into the cellular or sub-cellular level *in vivo* and *in situ*, much work has been done to extend the axial field of view using hardware, software or hybrid approaches, which can be briefly classified into the following categories.

1) *Multiple Foci*: Multi-foci method generates multiple focal regions aligned along the axial direction to form an extended axial focus with high resolution [27], [28]. Since the coherent transfer function (CTF) corresponding to each focus is optimal, the image resolution and contrast is equivalent to the in-focus image generated by a standard focusing scheme. Virtual source (Fig. 3) is an elegant method because the number of foci can

TABLE I
SUMMARY OF REPRESENTATIVE UHR-OCT SYSTEMS AT 800 NM

Ref.	Year	λ_c (nm)	Δz in air (μm)	Δz in tissue (μm)	Δx (μm)	Voxel size (μm^3)	Source type	Sample
[25]	1999	800	1.5	1.1	3	9.9	Ti:sapphire laser	African frog tadpole <i>in vivo</i>
[44]	2001	800	3.0	2.1	6	75.6	Ti:sapphire laser	Human retina <i>in vivo</i>
[45]	2002	761	2.2	1.7	5	42.5	SLDs	African frog tadpole <i>in vivo</i>
[46]	2002	725	0.75	0.5	2	2	Ti:sapphire laser	Human colorectal adenocarcinoma cells <i>in vitro</i>
[47]	2003	800	3.0	2.1	15-20	472.5-840	Ti:sapphire laser	Human eyes with diseases <i>in vivo</i>
[48]	2003	800	2.0	1.4	3	12.6	Ti:sapphire laser	Pig retina <i>in vitro</i>
[49]	2004	800	2.0	1.4	3	12.6	Ti:sapphire laser	Perfusion-fixed monkey fovea
[50]	2004	885	4.0	2.9	15	652.5	SLDs	Human retina <i>in vivo</i>
[51]	2004	800	3.0	2.1	5-10	52.5-210	Ti:sapphire laser	Human fovea <i>in vivo</i>
[52]	2004	890	3.2	2.3	5	57.5	SLDs	Human retina <i>in vivo</i> , Syrian golden hamster cheek pouch <i>in vivo</i>
[53]	2004	800	3.4	2.5	5	62.5	Ti:sapphire laser	Human retina <i>in vivo</i>
[54]	2004	850	3.0	2.1	15	472.5	Ti:sapphire laser	Human retina <i>in vivo</i>
[55]	2005	825	2.6	1.9	20	760	Ti:sapphire laser	Human retina <i>in vivo</i>
[56]	2006	800	3.0	2.1	6	75.6	SC	Fixed hamster cheek pouch
[57]	2006	825	2.8	2.0	5.6	62.7	Ti:sapphire laser	Mouse skin <i>in vivo</i>
[58]	2006	890	3.9	2.8	10	280	SLDs	Human retina <i>in vivo</i>
[59]	2006	800	2.4	1.7	10	170	Ti:sapphire laser	Mouse colon <i>in vivo</i>
[60]	2006	815	3.0	2.1	15-20	472.5-840	Ti:sapphire laser	Human retina <i>in vivo</i>
[61]	2008	800	2.8	2.0	3	18	Ti:sapphire laser	Cryosection of an adult human retina <i>in vivo</i>
[62]	2008	840	3.5	2.5	20	1000	SLDs	Human retina <i>in vivo</i>
[63]	2008	836	4.9	3.5	3.5	42.9	SLDs	Human retina <i>in vivo</i>
[64]	2009	840	4.9	3.5	15	787.5	SLDs	Human retina <i>in vivo</i>
[65]	2009	850	3.0	2.1	15	472.5	SLDs	Human retina <i>in vivo</i>
[66]	2010	825	2.7	2.0	5.6	62.7	Ti:sapphire laser	Esophagus tissue
[23]	2011	800	1.4	1.0	2	4	SC	Human coronary arterial tissue
[67]	2011	812.5	1.5	1.1	25	687.5	SC	Human cornea <i>in vivo</i>
[68]	2013	800	1.7	1.2	21	529.2	Ti:sapphire laser	Human precorneal tear film <i>in vivo</i>
[69]	2014	825	3.0	2.1	6.2	80.7	Ti:sapphire laser	Guinea pig esophagus <i>in vivo</i>
[70]	2014	927.5	1.3	0.93	1.7	2.7	SLDs	Zebra fish larvae <i>in vivo</i>
[71]	2016	840	2.7	1.9	5.5	57.5	SC	Human hearts <i>ex vivo</i>
[29]	2017	830	2.4	1.7	4	27.2	SC	Mouse trachea tissue
[72]	2017	800	1.3	0.95	4	15.2	SC	Human inferior limbus <i>in-vivo</i>
[21]	2017	800	1.2	0.86	20	344	Ti:sapphire laser	Human cornea <i>in vivo</i>
[24]	2017	820	2.4	1.7	6	61.2	Ti:sapphire laser	Mouse colon, rat esophagus, and small airways in sheep <i>in vivo</i>
[28]	2018	800	2.1	1.5	1.5	3.4	Femtolaser	Human cornea <i>in vivo</i>
[22]	2019	800	2.1	1.5	3-4	13.5-24	SC	Rabbit arteries <i>in vivo</i>
[73]	2019	760	2.0	1.4	10	140	SC	Human skin <i>in vivo</i>
[74]	2020	820	2.4	1.7	5.7	55.2	Ti:sapphire laser	Mouse brain <i>in vivo</i>

be scaled up without any fundamental issues [27]. The limitations are that the illumination path has to be in free space and the detection pinhole will reject out-of-detection-focus signals, causing sensitivity drop. Dual-foci method taking advantage of chromatic focal shift can double the axial focus of a fiber-optic probe but it suffers from axial resolution degradation due to the chromatic aberration [28]. A common problem of multi-foci methods is that only a part of total optical power is focused to a given axial point. The power efficiency is actually lower than the standard focusing scheme when the system is limited by the maximum permissible exposure.

2) *Focus Engineering*: This is a class of techniques that manipulate the pupil function of the focusing lens to generate a non-Gaussian focus. Center obscuration is the simplest one of this kind [23], [29], [30]. Typically, an annular aperture generates a quasi-Bessel focus, which is superresolving in the transverse direction and extended in the axial direction with respect to the Gaussian focus. Pure phase mask or phase pupil filters in combination with a spherical or GRIN lens are able to moderately extend the axial focus range at the expenses of a sensitivity drop of a few dBs [8], [31]–[33]. Axicon lens is also a

pure phase method, which is capable of extending the main-lobe axial range by more than 10 times [34], [35]. However, in a Bessel light field generated by an axicon lens most of the energy is diffracted to side-lobes so that the OCT sensitivity loss can be as large as 26 dB [35]; This sensitivity issue can be mitigated by use of Gaussian detection [35]. Few-mode interferometry also falls into this category. Instead of superimposing the diffraction patterns generated by all the concentric annular pupils in the same focal region in pure phase methods, this method uses ‘self-imaging’ of multimode fiber to shift the focus of each annular pupil to different axial locations, so that all the axial foci are fused to an axial focal range up to 1 mm with 2–3 μm transverse resolution (Fig. 4) [22], [36], [37].

It is common to all the focus engineering techniques that the CTF is sacrificed for axial focus extension since modulating the pupil function is essentially adding aberrations. Specifically, the angular frequency contents detected from each axial location is suboptimal, so that a significant amount of optical energy is ‘leaked’ to side-lobes resulting in sensitivity and contrast degradation. Therefore, the image quality is inferior to that of the standard focusing scheme with the same main-lobe FWHM.

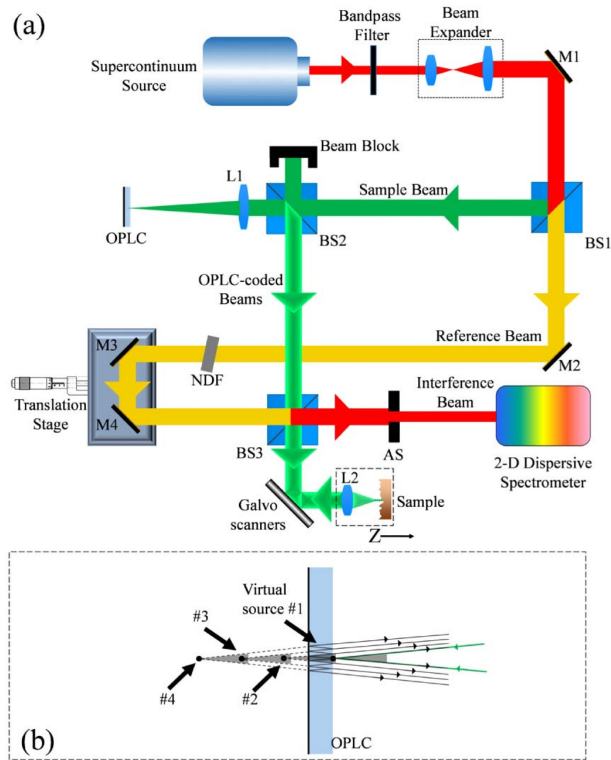


Fig. 3. (a) Schematic of multi-foci system based on virtual sources. M, mirror; BS, beam splitter; L, lens; OPLC, optical path length coder; NDF, neutral density filter; AS, aperture stop. (b) Virtual sources in OPLC. This figure is adopted from reference [27].

When characterizing the resolving power of a focusing scheme with suboptimal CTF, the main-lobe spot size should be evaluated together with sensitivity loss, Strehl ratio or encircled energy, and ratio between the side-lobe and main-lobe intensity [8], [33], [35].

3) *Digital Refocusing*: Digital refocusing methods take advantages of the fact that optical aberrations are recorded as the interferometric wavefront distortions optoelectronically in OCT signals. Correcting the defocus aberration digitally in the optical path delay (OPD) domain can extend the axial field of view by restoring the resolution and signal peak intensity. The forward model (FM) computes the phase error of each A-line with respect to a sample point based on the scalar diffraction model, and compensates these errors in OPD domain when reconstructing the OCT signal at the point [38]. Inverse scattering (IS) [39] and interferometric synthetic aperture microscopy (ISAM) [40] correct defocus by solving an inverse scattering problem. The sub-aperture correlation based digital adaptive optics (DAO) measures the phase error as the translation between the intensity of the images formed by the different subapertures with respect to intensity of the image formed by the central subaperture [41]–[43]. These computational approaches are elegant but all of them require wide-field imaging data and that a high phase-stability is maintained during wide-field scan, which is challenging for imaging dynamic cellular processes *in vivo*, especially in endoscopic scenarios. Physical sub-aperture approaches [75]–[77] acquire signals of all the sub-apertures within one A-line cycle, so that the phase stability between A-scans is not an issue.

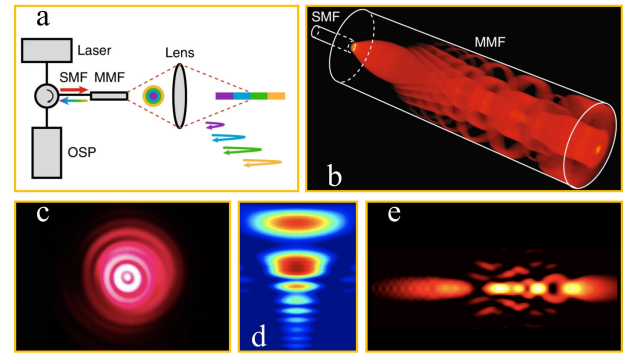


Fig. 4. (a) Sketch of few-mode interferometry. (b) 3D rendering of the intensity profile inside the multimode fiber. The transverse beam profile (c) and the simulated beam profile in top view (d) and side view (e). This figure is adopted from reference [22].

However, this approach suffers from the trade-off between the number of apertures and signal efficiency.

Digital refocusing methods don't degrade CTF so the image quality is equivalent to that of the standard focusing scheme. The additional technical features and limitations of this class of techniques are provided in the section below.

D. Aberration Correction

Imaging through thick tissues at cellular and subcellular resolution *in vivo* is highly challenging since optical aberrations result in not only the suboptimal coupling of signals at the detection pinhole but also interferometric wavefront distortions, which compromise both the coherence gating and the transverse focusing. Aberrations in OCT can be roughly classified into system aberrations and sample-induced aberrations. System aberrations are generally inherent effects arising due to the focusing optics, such as defocus and inevitable imperfections in the optics used in endoscopic applications [51], [78]. Sample-induced aberrations in turbid tissues generally vary spatially and temporally. They must be corrected before clear images of cells can be obtained *in vivo*.

The straightforward way to correct these aberrations is by using hardware-based adaptive optics (HAO), which measures the wavefront distortion and cancels it by modulating the incident light wavefront [79]. With an HAO correction, a set of correction parameters is valid only over a sufficiently small volume and over a sufficiently short period of time during which the sample-induced aberrations are constant. Consequently, it is time consuming to screen a large tissue volume [80], [81]. From a practical point of view, the system complexity and cost also impede its applications.

Optical aberrations are recorded as the interferometric wavefront distortions optoelectronically in OCT signals, which opens up the possibility of correcting the aberrations digitally. Wide-field computational techniques, including forward model [38], ISAM [39], [40], DAO [41]–[43], and computational adaptive optics (CAO) [82]–[84] have been developed to overcome the above-mentioned system complexity and speed issue with HAO. It has been demonstrated that above-mentioned computational methods enable cellular-resolution *in vivo* ophthalmic imaging

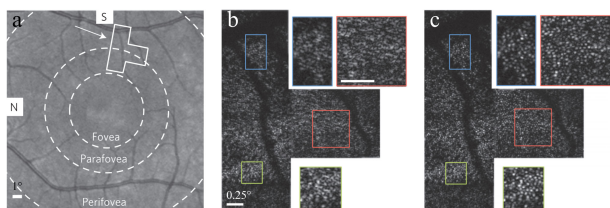


Fig. 5. (a) Scanning laser ophthalmoscope (SLO) image with the location of the cone photoreceptor mosaic outlined. (b) Raw *en face* OCT mosaic. (c) The same mosaic after computational aberration correction. Two insets are zoomed by 1.9 times. This figure is adopted from reference [82].

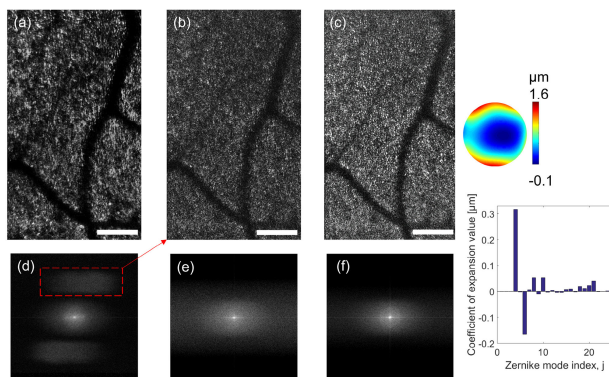


Fig. 6. Holographic line-field OCT with DAO. (a), shows an aberrated image of the photoreceptor acquired 7° from the fovea, (a) is the original *en face* image average over 5 frames (b) the OCT *en face* image over the same frames and (c) the corrected images after DAO. (d, e, f) show the respective Fourier planes with Yellot's rings well visible in (f). On the right side is the correction phase map and the corresponding Zernike coefficient plot of the phase map. The white scale bar indicates $200 \mu\text{m}$. This figure is adopted from reference [85].

without the need for HAO (Fig. 5) [82], [85]. To maintain a high phase stability over the full-field acquisitions, full-field mode [41]–[43], line-field mode (Fig. 6) [85], and Mega-Hz *en face* scanning mode [82], are often assumed, in addition to phase correction algorithms. The limitation is that all these high-speed imaging modes are implemented using time-domain OCT which is defective in sensitivity.

Digital refocusing by use of physical sub-apertures is able to correct aberrations using data acquired within a single A-line cycle [75]. Mo *et al.* divide the aperture of the objective lens central-symmetrically by wavefront and encode the OCT signal of each sub-aperture in OPD [75]. By dividing the amplitude, instead of the wavefront, of the sample beam, multiple aperture synthesis (MAS) operates with Gaussian beams and optimal fiber coupling efficiency. The sub-apertures are arranged linearly along the fast axis direction, so that the aberrations in OPD along the fast axis are compensated. The OCT signals of sub-apertures are acquired in two modes: time-encoded and OPD encoded (Fig. 7). The former is free of signal loss caused by beam splitters at the expense of acquisition speed [76]; the latter achieves optimal acquisition speed but suffers from signal loss at the beam splitters in the detection path and requires a large ranging depth of the spectrometer [86], [87].

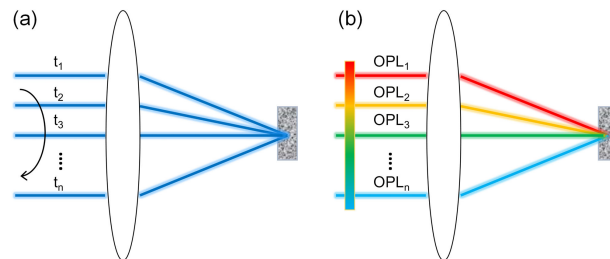


Fig. 7. Two types of beam divided manner, time-encoded (a) and optical path length (OPL) encoded (b).

E. Endoscopic and Intracoronary Fiber-Optic Probes

For endoscopic and intracoronary applications, the sample arm optics have to be miniaturized to conform to the space constraints of the lumen of the organ, endoscopic sheath or needle diameter. Ideally, the distal end optics should be implemented using a monolithic design to optimize the mechanical stabilities.

In general, the first fundamental problem with high resolution endoscopic or intracoronary OCT is the trade-off between the diameter of the focusing optics and the transverse spot size, given a fixed diameter of the lumen. Therefore, a fiber-optic probe has to maintain a relatively large diameter of 1–2 mm in order to achieve a transverse resolution of 2–3 μm [22], [29], [30], [36], [37], [89]. The second fundamental problem is the trade-off between the transverse spot size and the axial focal range which is inherent with all the HR-OCT. An axial focal ranging of 3–5 mm is normally needed for clinical applications but the diffraction limited axial focal range corresponding to a 2–3 μm transverse resolution is typically two orders of magnitude shorter. This problem is particularly important since in endoscopic and intracoronary applications the probe is often not centered and the lumen is non-circular in most cases. As a result, even the axial focal range is larger than the penetration depth ($\sim 2 \text{ mm}$) the tissue region of interest may still be out of focus during most time of scanning.

In addition, the choices for focusing optics are limited to ball lens and gradient index (GRIN) lens. Related with the focusing optics are aberrations including spherical aberrations, chromatic focal shifts, and astigmatism caused by the sheath [24], [90]–[92]. Ball lens typically assume spherical shape so that the spherical aberrations limit the achievable transverse resolution. For example, Yuan *et al.* achieved a transverse resolution of $6.2 \mu\text{m}$ at 830 nm with a ball lens diameter of $230 \mu\text{m}$ and a working distance of $545 \mu\text{m}$ [24]. The chromatic focal shift of ball lens can be well managed by use of a proper length of multimode fiber before the ball lens [24]. For more detailed information of ball lens probe design and fabrication, the readers are referred to reference [24], [90]. GRIN lens is more commonly used to achieve cellular resolution as the spherical aberrations are well managed in the lens design. However, chromatic focal shift is typically not well controlled in currently available GRIN lens so that axial resolution is degraded [28]. The astigmatism caused by the sheath can be managed by use of a cylindrical lens or cylindrical reflector [24], [90]–[92].

The first problem, trade-off between the diameter of the focusing optics and the transverse spot size, may be mitigated

by use of superresolving techniques, such as amplitude pupil filters (center obscuration) [29], [89] or phase pupil filters [32], [93], [94]. These approaches inevitably sacrifice image quality as discussed in Section C. This will still be a standing problem for endoscopic and intracoronary applications of HR-OCT.

There are more solutions to the second problem, the trade-off between the transverse spot size and the axial focal range. C-mode imaging is apparently not an option in this case. Dual-foci design is able to double the axial focal range by use of surplus in the spectral range of the input light, at the cost of system complexity [28]. Since supercontinuum source is required, it also suffers from the noise issue as mentioned in Section A. Amplitude pupil filter via center obscuration is commonly combined with a common path design, and superresolving main-lobe can be generated along an extended axial focus [29], [30], [89]. This design is very simple and it is relatively easy to realize the designed focus quality. As discussed in Section C, the expenses are degraded sensitivity and CTF. Phase pupil mask by means of binary phase filter [94], GRIN fiber or multimode fiber mode interference [31], [32] performs better in energy efficiency and side-lobe control than the amplitude pupil filter approach. However, it still suffers from sensitivity and CTF degradation. The above-mentioned approaches normally extended the axial focal range by no more than a few times. Therefore, they might be suitable for applications in small lumens where a large focal range is not required. Axial focus extension by use of few-mode interferometry is a promising approach since it makes it possible to obtain cross-sectional, cellular-resolution intravascular images of a 3-mm-diameter circular cylinder when spinning [22]. However, since the each annular zone carries a limited range angular frequency, this method inevitably suffers from sensitivity and CTF degradation [37].

IV. APPLICATIONS

A. Ophthalmic Imaging

OCT has become the standard-of-care tool for the assessment of most eye conditions. UHR-OCT has been primarily applied for ophthalmic imaging of both retina and the anterior segment. UHR-OCT enables superior visualization of tissue microstructure, including all major intraretinal layers in ophthalmic applications. Readers are referred to reference [10] for detailed review. Cellular resolution imaging can be readily achieved in the anterior segment since eye optics is not involved in focusing [26], [28], [95], [96]. Cellular resolution imaging of the posterior segment has to rely on technologies that can correct the aberrations of eye optics. With the advent of adaptive optics technologies, cellular resolution imaging of photoreceptors has been demonstrated [61], [97]. To overcome the drawbacks of adaptive optics, computational approaches, such as computational refocusing methods [82], [85], are also capable of achieve cellular resolution *in vivo*.

B. Coronary Atherosclerosis Imaging

Coronary atherosclerosis involves biological processes mediated by cells and extracellular components, including endothelium, leukocytes, macrophages, smooth muscle cells, platelets

and fibrin, occur on a microscopic scale [23]. The methods for imaging these cellular and extracellular components, unfortunately, are limited. With an axial resolution of 1 μm and a lateral resolution of 2 μm , it has been demonstrated that μOCT is capable of visualizing these structures in human arterial wall *ex vivo* (Fig. 2(c)) [22], [23], [99]–[101]. The detailed observations by μOCT are summarized in Table II. In addition, stent struts, polymer coating and presence of drug can also be seen in μOCT images *ex vivo* [23].

C. Respiratory Airway Imaging

Applications of high resolution OCT in respiratory airway imaging have been focused on mucociliary clearance (MCC) and related diseases such as cystic fibrosis (CF) airway disease, chronic obstructive pulmonary diseases (COPD) and primary ciliary dyskinesia (PCD). Healthy airway surfaces are lined by ciliated epithelial cells and covered with an airway surface layer (ASL), which has two components, a mucus layer that entraps inhaled particles and foreign pathogens, and a low viscosity periciliary layer (PCL) with a height of 7 μm , that lubricates airway surfaces and facilitates ciliary beating for efficient mucus clearance [104], [105]. Important parameters of MCC include ciliary beat frequency (CBF), mucus transport rate (MCT), ASL, and PCL. μOCT is the first method that can quantitatively measure these parameters in intact airway tissues under natural conditions [106]–[111], which makes it possible to study fundamental mechanisms that underlying MCC defects, disease mechanisms, and evaluate therapeutic strategies by measuring all the parameters of MCC in a single image *ex vivo* [106]–[109], [112]–[114]. More recently, trans-bronchoscopic μOCT devices have been developed to allow MCC assay in animal models and human *in vivo* (Fig. 8) [29], [30], [89].

D. Early-Stage Epithelial Cancer Detection

Precancerous lesions in epithelia are characterized by atypical changes at the subcellular, cellular and microstructural levels, such as atypical nuclear and cellular shape and atypical cellular arrangements. Detecting early-stage epithelial cancers and their precursor lesions are further complicated by the fact that lesions could be subtle and focally or heterogeneously distributed over large mucosal areas. HR-OCT is suitable for this task since the spatial resolutions matches the target features and it has the potential to scan a large mucosal area noninvasively *in situ* and *in vivo*.

The ability to identify cellular and subcellular structures relies on not only the spatial resolution but also the reflectance contrasts. There have been many studies reporting the reflectance contrast of cell nuclei in varieties of epithelial types and under different physiological conditions. The common feature is that the nuclear core is of low scattering, making it possible to clearly identify cell nuclei when the cytoplasm is of higher scattering [115]–[117]. In nonkeratinized squamous epithelial cells, the nucleocytoplasmic interfaces exhibit high scattering, so that nuclei can also be seen when the cytoplasm is of low scattering [116]. The scattering contrast of cytoplasm is dependent on the ultrastructural contents and arrangement of the cytoplasmic inclusions (Fig. 9). The readers are referred

TABLE II
SUMMARY OF μ OCT OBSERVATIONS OF CELLULAR AND EXTRACELLULAR COMPONENTS

Structures	Morphological features				μ OCT observations
	Size (μ m)	Shape	Nucleus	Cytoplasm	
Endothelial cell	Diameter: 10-20, thickness: 1-2	Flat, elongated	Round or elliptical	Scant	Cell boundary is high scattering with the cytoplasm low scattering; 3D μ OCT images show endothelial "pavementing" [23], [101]
Macrophage	20-50	Various, spherical, oval	Round or ellipsoidal	Abundant	Scattering, flocculent, round or ellipsoidal cells that were larger than monocytes; Nucleus: small, low scattering; Cytoplasm: large, high scattering [23], [102]
Red blood cells	Diameter: 6-8, thickness: 2-2.5	Biconcave discs	Absent	Nil	A pair of high reflective/scattering linear signals from the upper and lower cell boundary with $\sim 3.3 \mu$ m ($n = 1.36$) spacing in between [70]
Monocyte	12-20	Spherical	Round or oval	Abundant	Nucleus: small low scattering cytoplasm: abundant high scattering [23]
Neutrophil	12-15	Inactivated: spherical Activated: amorphous, amoeba-like	Band or segmented with 2-5 lobes	Sparse	Nucleus: multilobulated, low scattering; Cytoplasm: sparse high scattering [23], [103]
Lymphocyte	6-18		Large round	Scant	Small cells with scant cytoplasm; Nucleus: large low scattering; cytoplasm: scant high scattering [23]
Smooth muscle cell	Length: 50-200 Width: 2-8	Spindle	Large, cigar-shaped	Abundant	Phenotype 1: cell body with a low μ OCT signal intensity; Phenotype 2: a halo of low μ OCT signal surrounding a highly scattering interior [23]
Cholesterol crystal	Thickness: 2-3	Plates	NA	NA	High reflective interface between individual cholesterol crystals and surrounding tissue [23], [100]
Platelet	2-4	biconvex discoid	Absent	Nil	High scattering [23]

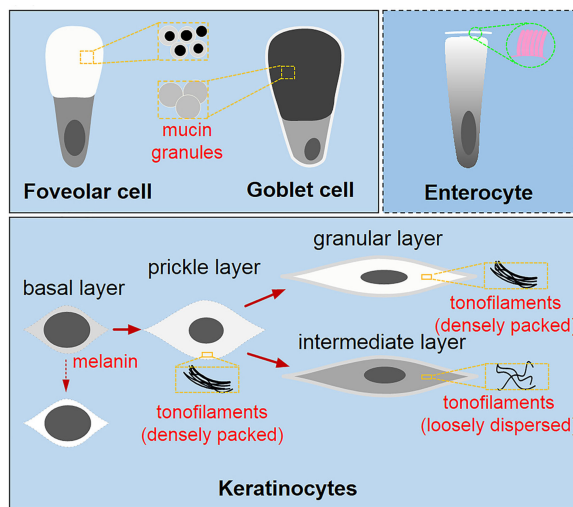
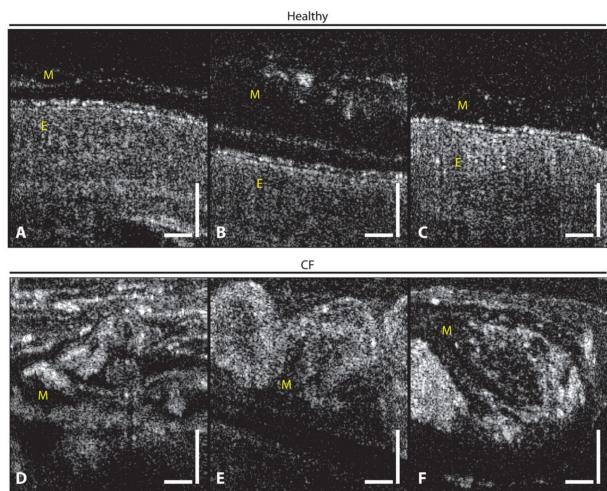


Fig. 8. Prominent and heterogeneous mucus reflectance intensity in CF subjects as compared to healthy non-CF controls. (A to C) Typical OCT images from healthy subjects showing continuous PCL, smooth epithelial surfaces, and a weakly scattering mucus layer above the ciliary layer. (D to F) Images from CF subjects showing highly reflective and heterogeneous mucus with distinctive structure accumulated to large thicknesses. View of the underlying epithelial tissue is obscured by mucus. Vertical and horizontal bars, 50 μ m. This figure is adopted from reference [30].

Fig. 9. Optical reflectance contrast models of foveolar cells, enterocytes and keratinocytes. This figure is adopted from reference [98].

to reference [98] for detailed information. Based on the understanding of subcellular reflectance contrast of cell nuclei and cytoplasm, certain types of pre-cancerous lesions can be identified using μ OCT, such as intestinal metaplasia in gastric mucosa, intraepithelial neoplasia in the nonkeratinized squamous epithelium, intestinal metaplasia in gastric mucosa (Fig. 10) and adenomatous polyps in colon (Fig. 11) [98].

V. DISCUSSIONS AND PERSPECTIVES

HR-OCT has the potential to provide cellular and subcellular level information of biological tissues that are only available

with excisional biopsy and histopathology. The unique capabilities of HR-OCT in understanding and diagnosis of ophthalmic disease, coronary atherosclerosis, respiratory airway disease, and epithelial cancers have been demonstrated by many studies.

Ophthalmic applications of HR-OCT have been focused on the distribution of photoreceptors in the *en face* view. Due to the aberrations of eye optics, hardware or computational adaptive optics techniques have to be used. Therefore, the application of HR-OCT in ophthalmology is hindered by the cost and complexity of hardware adaptive optics and the wide-field imaging mode employed for computational adaptive optics. Line-field OCT is able to provide both cross-sectional view and *en face* view of posterior segments and is a promising candidate for ophthalmic HR-OCT when working together with aberration correction methods.

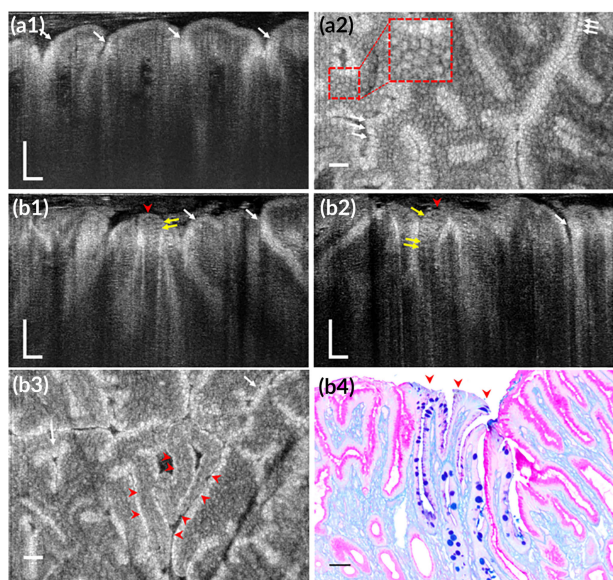


Fig. 10. Subcellular reflectance contrast of human gastric mucosa with intestinal metaplasia imaged by μ OCT *ex vivo*. (a1, a2) OCT cross-sectional (a1) and *en face* (a2) images of a specimen with normal mucosa and the white arrows indicates foveolar cells. (b1-b4) OCT cross-sectional (b1, b2) and *en face* images (b3) of another specimen from the region with intestinal metaplasia (red arrowheads): white arrows in (b1-b3) indicate foveolar cells and yellow arrows in (b1, b2) represent 'ectopic' goblet cells featured with low-scattering apical cytoplasm; corresponding pathology (b4) with PAS-AB mucin staining to highlight metaplastic area (red arrowheads). Scale bars, 50 μ m. This figure is adopted from reference [98].

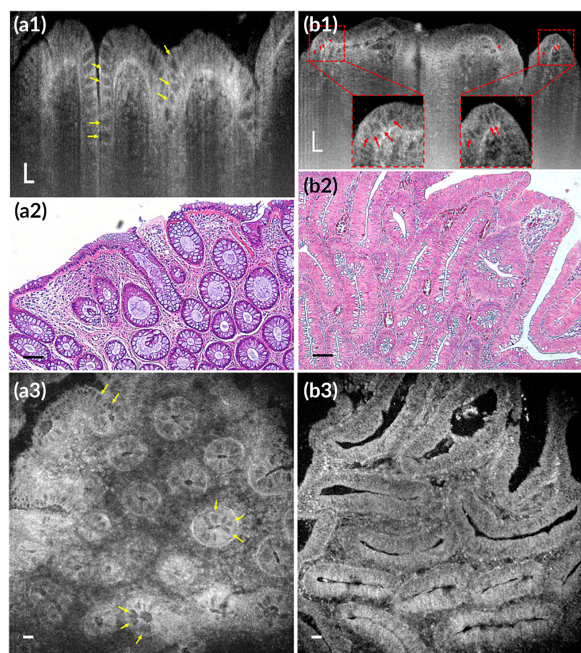


Fig. 11. Subcellular optical reflectance contrast of human colorectal polyps imaged by μ OCT *ex vivo*. (a1-a3) Representative μ OCT cross-sectional image (a1), corresponding H&E stained histology (a2) and *en face* μ OCT view (a3) of a hyperplastic polyp. (b1-b3) Representative μ OCT cross-sectional image (b1), corresponding H&E stained histology (b2) and *en face* μ OCT view (b3) of an adenomatous polyp. Yellow arrows represent goblet cells and red arrows indicate low-scattering nuclei. Scale bars, 50 μ m. This figure is adopted from reference [98].

HR-OCT is particularly important for intracoronary use because currently there is no way to image arterial wall at the cellular or subcellular resolution. The good news is that many important cellular and extracellular structures involved in atherosclerosis and intracoronary intervention are relatively large in transverse direction, which partly relieves the requirement of transverse resolution. In endoscopic and intracoronary applications, most of the study demonstrated so far are in animal models and human tissues *ex vivo*, because there are fundamental issues in realizing cellular resolution in fiber optical probes. Although a number of technique have been demonstrated, each of them suffers from one or more inherent trade-offs. One of the main obstacles is that OCT is operated within the single mode regime, leaving little room to correct aberrations without compromising other performances. Few mode interferometry opens up a new door as multiple fiber modes provide more flexibility to tackle the CTF and energy efficiency issues.

Given the fact that it will take more efforts and time to tackle the fundamental problems with HR-OCT for existing endoscopic and intracoronary application, the current research might be focused on applications where a large axial field of view and working distance are not critical, for example, endoscopic imaging of small luminal organs and needle based imaging of solid organs. For these applications, the current focus extension and aberration correction methods might suffice.

REFERENCES

- [1] D. Huang *et al.*, "Optical coherence tomography," *Science*, vol. 254, pp. 1178–1181, 1991.
- [2] S. S. Gao *et al.*, "Optical coherence tomography angiography," *Invest. Ophthalmol. Vis. Sci.*, vol. 57, pp. OCT27–OCT36, 2016.
- [3] J. Wang, D. Fonn, T. L. Simpson, and L. Jones, "Precorneal and pre-and postlens tear film thickness measured indirectly with optical coherence tomography," *Invest. Ophthalmol. Vis. Sci.*, vol. 44, pp. 2524–2528, 2003.
- [4] R. A. Leitgeb *et al.*, "Real-time measurement of in vitro flow by Fourier-domain color Doppler optical coherence tomography," *Opt. Lett.*, vol. 29, pp. 171–173, 2004.
- [5] J. F. De Boer, T. E. Milner, M. J. Van Gemert, and J. S. Nelson, "Two-dimensional birefringence imaging in biological tissue by polarization-sensitive optical coherence tomography," *Opt. Lett.*, vol. 22, pp. 934–936, 1997.
- [6] U. Morgner *et al.*, "Spectroscopic optical coherence tomography," *Opt. Lett.*, vol. 25, pp. 111–113, 2000.
- [7] J. M. Schmitt, "OCT elastography: Imaging microscopic deformation and strain of tissue," *Opt. Exp.*, vol. 3, pp. 199–211, 1998.
- [8] L. Liu, C. Liu, W. C. Howe, C. Sheppard, and N. Chen, "Binary-phase spatial filter for real-time swept-source optical coherence microscopy," *Opt. Lett.*, vol. 32, pp. 2375–2377, 2007.
- [9] M. Zhang, Z. Ren, and P. Yu, "Improve depth of field of optical coherence tomography using finite energy airy beam," *Opt. Lett.*, vol. 44, pp. 3158–3161, 2019.
- [10] W. Drexler and J. G. Fujimoto, *Optical Coherence Tomography: Technology and Applications*. Berlin, Germany: Springer, 2008.
- [11] S. Yun, G. Tearney, B. Bouma, B. Park, and J. de Boer, "High-speed spectral-domain optical coherence tomography at 1.3 μ m wavelength," *Opt. Exp.*, vol. 11, pp. 3598–3604, 2003.
- [12] M. A. Choma, M. V. Sarunic, C. Yang, and J. A. Izatt, "Sensitivity advantage of swept source and Fourier domain optical coherence tomography," *Opt. Exp.*, vol. 11, pp. 2183–2189, 2003.
- [13] R. Leitgeb, C. Hitzenberger, and A. F. Fercher, "Performance of Fourier domain vs. time domain optical coherence tomography," *Opt. Exp.*, vol. 11, pp. 889–894, 2003.
- [14] G. Haeusler and M. Lindner, "Coherence radar' and 'Spectral radar'- new tools for dermatological diagnosis," *J. Biomed. Opt.*, vol. 3, pp. 21–31, 1998.

- [15] Z. Hu, Y. Pan, and A. M. Rollins, "Analytical model of spectrometer-based two-beam spectral interferometry," *Appl Opt.*, vol. 46, pp. 8499–8505, 2007.
- [16] K. Bizheva *et al.*, "Compact, broad-bandwidth fiber laser for sub-2- μm axial resolution optical coherence tomography in the 1300-nm wavelength region," *Opt. Lett.*, vol. 28, pp. 707–709, 2003.
- [17] S. P. Chong, M. Bernucci, H. Radhakrishnan, and V. J. Srinivasan, "Structural and functional human retinal imaging with a fiber-based visible light OCT ophthalmoscope," *Biomed. Opt. Exp.*, vol. 8, pp. 323–337, 2017.
- [18] A. Lichtenegger *et al.*, "Spectroscopic imaging with spectral domain visible light optical coherence microscopy in alzheimer's disease brain samples," *Biomed. Opt. Exp.*, vol. 8, pp. 4007–4025, 2017.
- [19] D. J. Harper *et al.*, "White light polarization sensitive optical coherence tomography for sub-micron axial resolution and spectroscopic contrast in the murine retina," *Biomed. Opt. Exp.*, vol. 9, pp. 2115–2129, 2018.
- [20] J. Yi, S. Chen, V. Backman, and H. F. Zhang, "In vivo functional microangiography by visible-light optical coherence tomography," *Biomed. Opt. Exp.*, vol. 5, pp. 3603–3612, 2014.
- [21] R. M. Werkmeister *et al.*, "Ultrahigh-resolution OCT imaging of the human cornea," *Biomed. Opt. Exp.*, vol. 8, pp. 1221–1239, 2017.
- [22] B. Yin *et al.*, "3D cellular-resolution imaging in arteries using few-mode interferometry," *Light: Sci. Appl.*, vol. 8, pp. 1–9, 2019.
- [23] L. Liu *et al.*, "Imaging the subcellular structure of human coronary atherosclerosis using micro-optical coherence tomography," *Nat. Med.*, vol. 17, 2011, Art. no. 1010.
- [24] W. Yuan, R. Brown, W. Mitzner, L. Yarmus, and X. Li, "Super-achromatic monolithic microprobe for ultrahigh-resolution endoscopic optical coherence tomography at 800 nm," *Nat. Commun.*, vol. 8, 2017, Art. no. 1531.
- [25] W. Drexler *et al.*, "In vivo ultrahigh-resolution optical coherence tomography," *Opt. Lett.*, vol. 24, pp. 1221–1223, 1999.
- [26] S. Chen *et al.*, "Visualizing micro-anatomical structures of the posterior cornea with micro-optical coherence tomography," *Sci. Rep.*, vol. 7, 2017, Art. no. 10752.
- [27] W. Bao, Z. Ding, J. Qiu, Y. Shen, P. Li, and Z. Chen, "Quasi-needle-like focus synthesized by optical coherence tomography," *Opt. Lett.*, vol. 42, pp. 1385–1388, 2017.
- [28] B. Tan, Z. Hosseinaee, L. Han, O. Kralj, L. Sorbara, and K. Bizheva, "250 kHz, 1.5 μm resolution SD-OCT for in-vivo cellular imaging of the human cornea," *Biomed. Opt. Exp.*, vol. 9, pp. 6569–6583, 2018.
- [29] D. Cui *et al.*, "Flexible, high-resolution micro-optical coherence tomography endobronchial probe toward in vivo imaging of cilia," *Opt. Lett.*, vol. 42, pp. 867–870, 2017.
- [30] H. M. Leung *et al.*, "Intranasal micro-optical coherence tomography imaging for cystic fibrosis studies," *Sci. Transl. Med.*, vol. 11, 2019, Art. no. eaav3505.
- [31] D. Lorensen, X. Yang, and D. D. Sampson, "Ultrathin fiber probes with extended depth of focus for optical coherence tomography," *Opt. Lett.*, vol. 37, pp. 1616–1618, 2012.
- [32] J. Qiu, T. Han, Z. Liu, J. Meng, and Z. Ding, "Uniform focusing with an extended depth range and increased working distance for optical coherence tomography by an ultrathin monolith fiber probe," *Opt. Lett.*, vol. 45, pp. 976–979, 2020.
- [33] L. Liu *et al.*, "Superresolution along extended depth of focus with binary-phase filters for the Gaussian beam," *J. Opt. Soc. Amer. A*, vol. 25, pp. 2095–2101, 2008.
- [34] Z. Ding, H. Ren, Y. Zhao, J. S. Nelson, and Z. Chen, "High-resolution optical coherence tomography over a large depth range with an axicon lens," *Opt. Lett.*, vol. 27, pp. 243–245, 2002.
- [35] R. Leitgeb, M. Villiger, A. Bachmann, L. Steinmann, and T. Lasser, "Extended focus depth for Fourier domain optical coherence microscopy," *Opt. Lett.*, vol. 31, pp. 2450–2452, 2006.
- [36] B. Yin, K. K. Chu, C.-P. Liang, K. Singh, R. Reddy, and G. J. Tearney, " μOCT imaging using depth of focus extension by self-imaging wavefront division in a common-path fiber optic probe," *Opt. Exp.*, vol. 24, pp. 5555–5564, 2016.
- [37] B. Yin, C. Hyun, J. A. Gardecki, and G. J. Tearney, "Extended depth of focus for coherence-based cellular imaging," *Optica*, vol. 4, pp. 959–965, 2017.
- [38] Y. Yasuno *et al.*, "Non-iterative numerical method for laterally super-resolving Fourier domain optical coherence tomography," *Opt. Exp.*, vol. 14, pp. 1006–1020, 2006.
- [39] D. L. Marks, T. S. Ralston, S. A. Boppart, and P. S. Carney, "Inverse scattering for frequency-scanned full-field optical coherence tomography," *JOSA A*, vol. 24, pp. 1034–1041, 2007.
- [40] T. S. Ralston, D. L. Marks, P. S. Carney, and S. A. Boppart, "Interferometric synthetic aperture microscopy," *Nat. Phys.*, vol. 3, pp. 129–134, 2007.
- [41] A. Kumar, W. Drexler, and R. A. Leitgeb, "Numerical focusing methods for full field OCT: A comparison based on a common signal model," *Opt. Exp.*, vol. 22, pp. 16061–16078, 2014.
- [42] A. Kumar, W. Drexler, and R. A. Leitgeb, "Subaperture correlation based digital adaptive optics for full field optical coherence tomography," *Opt. Exp.*, vol. 21, pp. 10850–10866, 2013.
- [43] L. Ginner *et al.*, "Noniterative digital aberration correction for cellular resolution retinal optical coherence tomography in vivo," *Optica*, vol. 4, pp. 924–931, 2017.
- [44] W. Drexler, U. Morgner, R. K. Ghanta, F. X. Kärtner, J. S. Schuman, and J. G. Fujimoto, "Ultrahigh-resolution ophthalmic optical coherence tomography," *Nat. Med.*, vol. 7, pp. 502–507, 2001.
- [45] A. M. Kowalevich, T. Ko, I. Hartl, J. G. Fujimoto, M. Pollnau, and R. P. Salathé, "Ultrahigh resolution optical coherence tomography using a superluminescent light source," *Opt. Exp.*, vol. 10, pp. 349–353, 2002.
- [46] B. Povazay *et al.*, "Submicrometer axial resolution optical coherence tomography," *Opt. Lett.*, vol. 27, pp. 1800–1802, 2002.
- [47] W. Drexler *et al.*, "Enhanced visualization of macular pathology with the use of ultrahigh-resolution optical coherence tomography," *Arch. Ophthalmol.*, vol. 121, pp. 695–706, 2003.
- [48] M. Gloesmann, B. Hermann, C. Schubert, H. Sattmann, P. K. Ahnelt, and W. Drexler, "Histologic correlation of pig retina radial stratification with ultrahigh-resolution optical coherence tomography," *Invest. Ophthalmol. Vis. Sci.*, vol. 44, pp. 1696–1703, 2003.
- [49] E. M. Anger *et al.*, "Ultrahigh resolution optical coherence tomography of the monkey fovea. Identification of retinal sublayers by correlation with semithin histology sections," *Exp. Eye Res.*, vol. 78, pp. 1117–1125, 2004.
- [50] B. Cense *et al.*, "Ultrahigh-resolution high-speed retinal imaging using spectral-domain optical coherence tomography," *Opt. Exp.*, vol. 12, pp. 2435–2447, 2004.
- [51] B. Hermann *et al.*, "Adaptive-optics ultrahigh-resolution optical coherence tomography," *Opt. Lett.*, vol. 29, pp. 2142–2144, 2004.
- [52] T. H. Ko *et al.*, "Ultrahigh resolution optical coherence tomography imaging with a broadband superluminescent diode light source," *Opt. Exp.*, vol. 12, pp. 2112–2119, Sep. 2004.
- [53] R. Leitgeb *et al.*, "Ultrahigh resolution Fourier domain optical coherence tomography," *Opt. Exp.*, vol. 12, pp. 2156–2165, 2004.
- [54] M. Wojtkowski, V. J. Srinivasan, T. H. Ko, J. G. Fujimoto, A. Kowalczyk, and J. S. Duker, "Ultrahigh-resolution, high-speed, Fourier domain optical coherence tomography and methods for dispersion compensation," *Opt. Exp.*, vol. 12, pp. 2404–2422, 2004.
- [55] M. Wojtkowski *et al.*, "Three-dimensional retinal imaging with high-speed ultrahigh-resolution optical coherence tomography," *Ophthalmology*, vol. 112, pp. 1734–1746, 2005.
- [56] A. D. Aguirre, N. Nishizawa, J. G. Fujimoto, W. Seitz, M. Lederer, and D. Kopf, "Continuum generation in a novel photonic crystal fiber for ultrahigh resolution optical coherence tomography at 800 nm and 1300 nm," *Opt. Exp.*, vol. 14, pp. 1145–1160, 2006.
- [57] M. J. Cobb, Y. Chen, R. A. Underwood, M. L. Usui, J. Olerud, and X. Li, "Noninvasive assessment of cutaneous wound healing using ultrahigh-resolution optical coherence tomography," *J. Biomed. Opt.*, vol. 11, 2006, Art. no. 064002.
- [58] V. Srinivasan, M. Wojtkowski, J. Fujimoto, and J. Duker, "In vivo measurement of retinal physiology with high-speed ultrahigh-resolution optical coherence tomography," *Opt. Lett.*, vol. 31, pp. 2308–2310, 2006.
- [59] A. R. Tumlinson *et al.*, "Endoscope-tip interferometer for ultrahigh," *Opt. Exp.*, vol. 14, pp. 1878–1887, 2006.
- [60] A. J. Witkin *et al.*, "Redefining lamellar holes and the vitreomacular interface: An ultrahigh-resolution optical coherence tomography study," *Ophthalmology*, vol. 113, pp. 388–397, 2006.
- [61] E. J. Fernández *et al.*, "Ultrahigh resolution optical coherence tomography and pancorrection for cellular imaging of the living human retina," *Opt. Exp.*, vol. 16, pp. 11083–11094, 2008.
- [62] V. J. Srinivasan *et al.*, "Characterization of outer retinal morphology with high-speed, ultrahigh-resolution optical coherence tomography," *Invest. Ophthalmol. Vis. Sci.*, vol. 49, pp. 1571–1579, 2008.
- [63] R. J. Zawadzki, B. Cense, Y. Zhang, S. S. Choi, D. T. Miller, and J. S. Werner, "Ultrahigh-resolution optical coherence tomography with monochromatic and chromatic aberration correction," *Opt. Exp.*, vol. 16, pp. 8126–8143, 2008.
- [64] Y. Chen *et al.*, "Three-dimensional ultrahigh resolution optical coherence tomography imaging of age-related macular degeneration!" *Opt. Exp.*, vol. 17, 2009, Art. no. 4046.
- [65] M. Hangai, M. Yamamoto, A. Sakamoto, and N. Yoshimura, "Ultrahigh-resolution versus speckle noise-reduction in spectral-domain optical coherence tomography," *Opt. Exp.*, vol. 17, pp. 4221–4235, 2009.

- [66] M. J. Cobb *et al.*, "Imaging of subsquamous barrett's epithelium with ultrahigh-resolution optical coherence tomography: A histologic correlation study," *Gastrointestinal Endoscopy*, vol. 71, pp. 223–230, 2010.
- [67] R. Yadav, K.-S. Lee, J. P. Rolland, J. M. Zavislan, J. V. Aquavella, and G. Yoon, "Micrometer axial resolution OCT for corneal imaging," *Biomed. Opt. Exp.*, vol. 2, pp. 3037–3046, 2011.
- [68] R. M. Werkmeister *et al.*, "Measurement of tear film thickness using ultrahigh-resolution optical coherence tomography," *Invest. Ophthalmol. Vis. Sci.*, vol. 54, pp. 5578–5583, 2013.
- [69] J. Xi *et al.*, "Diffractive catheter for ultrahigh-resolution spectral-domain volumetric OCT imaging," *Opt. Lett.*, vol. 39, pp. 2016–2019, 2014.
- [70] D. Cui *et al.*, "Dual spectrometer system with spectral compounding for 1- μm optical coherence tomography in vivo," *Opt. Lett.*, vol. 39, pp. 6727–6730, 2014.
- [71] X. Yao, Y. Gan, C. C. Marboe, and C. P. Hendon, "Myocardial imaging using ultrahigh-resolution spectral domain optical coherence tomography," *J. Biomed. Opt.*, vol. 21, 2016, Art. no. 061006.
- [72] K. Bizheva *et al.*, "In-vivo imaging of the palisades of vogt and the limbal crypts with sub-micrometer axial resolution optical coherence tomography," *Biomed. Opt. Exp.*, vol. 8, pp. 4141–4151, 2017.
- [73] T.-A. Wang, M.-C. Chan, H.-C. Lee, C.-Y. Lee, and M.-T. Tsai, "Ultrahigh-resolution optical coherence tomography/angiography with an economic and compact supercontinuum laser," *Biomed. Opt. Exp.*, vol. 10, pp. 5687–5702, 2019.
- [74] W. Yuan *et al.*, "Theranostic OCT microneedle for fast ultrahigh-resolution deep-brain imaging and efficient laser ablation in vivo," *Sci. Adv.*, vol. 6, 2020, Art. no. eaaz9664.
- [75] J. Mo, M. de Groot, and J. F. de Boer, "Focus-extension by depth-encoded synthetic aperture in optical coherence tomography," *Opt. Exp.*, vol. 21, pp. 10048–10061, 2013.
- [76] E. Bo *et al.*, "Depth-of-focus extension in optical coherence tomography via multiple aperture synthesis," *Optica*, vol. 4, pp. 701–706, 2017.
- [77] J. Mo, M. de Groot, and J. F. de Boer, "Depth-encoded synthetic aperture optical coherence tomography of biological tissues with extended focal depth," *Opt. Exp.*, vol. 23, pp. 4935–4945, 2015.
- [78] W. A. Benalcazar, W. Jung, and S. A. Boppart, "Aberration characterization for the optimal design of high-resolution endoscopic optical coherence tomography catheters," *Opt. Lett.*, vol. 37, pp. 1100–1102, 2012.
- [79] I. M. Vellekoop, A. Lagendijk, and A. Mosk, "Exploiting disorder for perfect focusing," *Nat. Photon.*, vol. 4, pp. 320–322, 2010.
- [80] R. J. Zawadzki *et al.*, "Adaptive-optics optical coherence tomography for high-resolution and high-speed 3D retinal in vivo imaging," *Opt. Exp.*, vol. 13, pp. 8532–8546, 2005.
- [81] J. Jang *et al.*, "Complex wavefront shaping for optimal depth-selective focusing in optical coherence tomography," *Opt. Exp.*, vol. 21, pp. 2890–2902, 2013.
- [82] N. D. Shemonski, F. A. South, Y.-Z. Liu, S. G. Adie, P. S. Carney, and S. A. Boppart, "Computational high-resolution optical imaging of the living human retina," *Nat. Photon.*, vol. 9, pp. 440–443, 2015.
- [83] S. G. Adie, B. W. Graf, A. Ahmad, P. S. Carney, and S. A. Boppart, "Computational adaptive optics for broadband optical interferometric tomography of biological tissue," *Proc. Nat. Acad. Sci.*, vol. 109, pp. 7175–7180, 2012.
- [84] A. Ahmad *et al.*, "Real-time in vivo computed optical interferometric tomography," *Nat. Photon.*, vol. 7, pp. 444–448, 2013.
- [85] L. Ginner *et al.*, "Holographic line field en-face OCT with digital adaptive optics in the retina in vivo," *Biomed. Opt. Exp.*, vol. 9, pp. 472–485, 2018.
- [86] E. Bo *et al.*, "Cellular-resolution in vivo tomography in turbid tissue through digital aberration correction," *Photonix*, vol. 1, 2020, Art. no. 9.
- [87] E. Bo, X. Ge, X. Yu, J. Mo, and L. Liu, "Extending axial focus of optical coherence tomography using parallel multiple aperture synthesis," *Appl. Opt.*, vol. 57, pp. 3556–3560, 2018.
- [88] D. Cui *et al.*, "Multifiber angular compounding optical coherence tomography for speckle reduction," *Opt. Lett.*, vol. 42, pp. 125–128, 2017.
- [89] K. K. Chu *et al.*, "In vivo imaging of airway cilia and mucus clearance with micro-optical coherence tomography," *Biomed. Opt. Exp.*, vol. 7, pp. 2494–2505, 2016.
- [90] M. J. Gora, M. J. Suter, G. J. Tearney, and X. Li, "Endoscopic optical coherence tomography: Technologies and clinical applications [Invited]," *Biomed. Opt. Exp.*, vol. 8, pp. 2405–2444, 2017.
- [91] J. Xi, L. Huo, Y. Wu, M. J. Cobb, J. H. Hwang, and X. Li, "High-resolution OCT balloon imaging catheter with astigmatism correction," *Opt. Lett.*, vol. 34, pp. 1943–1945, 2009.
- [92] M. Woo Lee, Y. Hoon Kim, J. Xing, and H. Yoo, "Astigmatism-corrected endoscopic imaging probe for optical coherence tomography using soft lithography," *Opt. Lett.*, vol. 45, pp. 4867–4870, 2020.
- [93] B. C. Quirk, R. A. McLaughlin, A. Curatolo, R. W. Kirk, D. D. Sampson, and P. B. Noble, "In situ imaging of lung alveoli with an optical coherence tomography needle probe," *J. Biomed. Opt.*, vol. 16, 2011, Art. no. 036009.
- [94] J. Kim, J. Xing, H. S. Nam, J. W. Song, J. W. Kim, and H. Yoo, "Endoscopic micro-optical coherence tomography with extended depth of focus using a binary phase spatial filter," *Opt. Lett.*, vol. 42, pp. 379–382, 2017.
- [95] X. Yao *et al.*, "In vivo corneal endothelium imaging using ultrahigh resolution OCT," *Biomed. Opt. Exp.*, vol. 10, pp. 5675–5686, 2019.
- [96] A. Wartak, M. S. Schenk, V. Bühler, S. A. Kassumeh, R. Birngruber, and G. J. Tearney, "Micro-optical coherence tomography for high-resolution morphologic imaging of cellular and nerval corneal micro-structures," *Biomed. Opt. Exp.*, vol. 11, pp. 5920–5933, 2020.
- [97] R. J. Zawadzki, S. S. Choi, A. R. Fuller, J. W. Evans, B. Hamann, and J. S. Werner, "Cellular resolution volumetric in vivo retinal imaging with adaptive optics-optical coherence tomography," *Opt. Exp.*, vol. 17, pp. 4084–4094, 2009.
- [98] S. Chen *et al.*, "Understanding optical reflectance contrast for real-time characterization of epithelial precursor lesions," *Bioeng. Transl. Med.*, vol. 4, 2019, Art. no. e10137.
- [99] Y. Luo *et al.*, "Modeling of mechanical stress exerted by cholesterol crystallization on atherosclerotic plaques," *PLOS ONE*, vol. 11, 2016, Art. no. e0155117.
- [100] Y. Luo *et al.*, "Imaging cellular structures of atherosclerotic coronary arteries using circumferentially scanning micro-optical coherence tomography fiber probe ex vivo," *IEEE Access*, vol. 6, pp. 62988–62994, 2018.
- [101] K. Nishimiya *et al.*, "Micro-optical coherence tomography for endothelial cell visualization in the coronary arteries," *JACC: Cardiovasc. Imag.*, vol. 12, pp. 1878–1880, 2019.
- [102] M. Kashiwagi *et al.*, "Feasibility of the assessment of cholesterol crystals in human macrophages using micro optical coherence tomography," *PLOS ONE*, vol. 9, 2014, Art. no. e102669.
- [103] K. K. Chu *et al.*, "Illuminating dynamic neutrophil trans-epithelial migration with micro-optical coherence tomography," *Sci. Rep.*, vol. 7, 2017, Art. no. 45789.
- [104] M. R. Knowles and R. C. Boucher, "Mucus clearance as a primary innate defense mechanism for mammalian airways," *J. Clin. Investigation*, vol. 109, pp. 571–577, 2002.
- [105] R. Boucher, "New concepts of the pathogenesis of cystic fibrosis lung disease," *Eur. Respir. J.*, vol. 23, pp. 146–158, 2004.
- [106] L. Liu *et al.*, "Method for quantitative study of airway functional microanatomy using micro-optical coherence tomography," *PLOS ONE*, vol. 8, 2013, Art. no. e54473.
- [107] S. E. Birket *et al.*, "A functional anatomic defect of the cystic fibrosis airway," *Amer. J. Respir. Crit. Care Med.*, vol. 190, pp. 421–432, 2014.
- [108] L. Liu *et al.*, "An autoregulatory mechanism governing mucociliary transport is sensitive to mucus load," *Amer. J. Respir. Cell Mol. Biol.*, vol. 51, pp. 485–493, 2014.
- [109] A. L. Oldenburg, R. K. Chhetri, D. B. Hill, and B. Button, "Monitoring airway mucus flow and ciliary activity with optical coherence tomography," *Biomed. Opt. Exp.*, vol. 3, pp. 1978–1992, 2012.
- [110] K. K. Chu *et al.*, "Particle-Tracking microrheology using micro-optical coherence tomography," *Biophysical J.*, vol. 111, pp. 1053–1063, 2016.
- [111] X. Ge *et al.*, "Geometry-Dependent spectroscopic contrast in deep tissues," *iScience*, vol. 19, pp. 965–975, 2019.
- [112] V. Y. Lin *et al.*, "Excess mucus viscosity and airway dehydration impact COPD airway clearance," *Eur. Respir. J.*, vol. 55, 2020, Art. no. 1900419.
- [113] S. V. Raju *et al.*, "The cystic fibrosis transmembrane conductance regulator potentiator ivacaftor augments mucociliary clearance abrogating cystic fibrosis transmembrane conductance regulator inhibition by cigarette smoke," *Amer. J. Respir. Cell Mol. Biol.*, vol. 56, pp. 99–108, 2017.
- [114] S. E. Birket *et al.*, "Combination therapy with cystic fibrosis transmembrane conductance regulator modulators augment the airway functional microanatomy," *Amer. J. Physiol.-Lung Cellular Mol. Physiol.*, vol. 310, pp. L928–L939, 2016.
- [115] S. Tang, C.-H. Sun, T. B. Krasieva, Z. Chen, and B. J. Tromberg, "Imaging subcellular scattering contrast by using combined optical coherence and multiphoton microscopy," *Opt. Lett.*, vol. 32, pp. 503–505, 2007.
- [116] S. Chen *et al.*, "Contrast of nuclei in stratified squamous epithelium in optical coherence tomography images at 800 nm," *J. Biophoton.*, vol. 12, Art. no. e201900073, Sep 2019.
- [117] Y. Pan, Z. Wu, Z. Yuan, Z. G. Wang, and C. W. Du, "Subcellular imaging of epithelium with time-lapse optical coherence tomography," *J. Biomed. Opt.*, vol. 12, 2007, Art. no. 050504.

Xin Ge received the B.S. degree in optics and the Ph.D. degree in synchrotron radiation and its applications from the University of Science and Technology of China, Hefei, China, in 2008 and 2013, respectively. From 2013 to 2015, he was a Research Fellow at The Chinese University of Hong Kong, Hong Kong. He is currently a Research Fellow with Nanyang Technological University, Singapore. His current research interests include high-resolution optical coherence tomography, spectroscopic optical coherence tomography, X-ray imaging, and related medical applications.

Shufen Chen was born in Guangdong, China, in 1987. She received the bachelor's degree in medicine from Southern Medical University, Guangzhou, China, in 2011 and the master's degree in internal medicine from Sun Yat-Sen University, Guangzhou, China, in 2014. Since 2020, she has been working toward the Ph.D. degree with the School of Biomedical Sciences, The Chinese University of Hong Kong, Hong Kong. From 2014 to 2016, she was at Sun Yat-Sen Memorial Hospital, Guangzhou, China, as a Physician. During 2016-2020, she was a Research Associate at the School of Electrical and Electronic Engineering, Nanyang Technological University, Singapore. Her research interests include the cancer diagnosis and cancer therapy.

Si Chen received the bachelor's degree in clinical medicine from Zhengzhou University, Zhengzhou, China, in 2011, the master's degree in ophthalmology from Peking University, Beijing, China, in 2014, and the Ph.D. degree in bioengineering from Nanyang Technological University, Singapore, in 2020. From 2014 to 2015, she was a Research Associate and since 2020, a Research Fellow with the School of Electrical and Electronic Engineering, Nanyang Technological University. Her research interests include disease prevention and early diagnosis with noninvasive optical imaging tools.

Linbo Liu (Member, IEEE) was born in Yulin, Shaanxi, China, in 1978. He received the B.Eng. degree in measurement and control technology, and instrumentation, the M.Eng. degree in optical engineering from Tianjing University, Tianjing, China, in 2004, and the Ph.D. degree in bioengineering from the National University of Singapore, Singapore, in 2009. From 2009 to 2012, he was a Research Fellow and an Instructor at the Wellman Center for Photomedicine, Massachusetts General Hospital and Harvard Medical School, Boston, MA, USA. Since 2012, he has been an Assistant Professor and an Associate Professor with the School of Electrical and Electronic Engineering, and with the School of Chemical and Biomedical Engineering, respectively, Nanyang Technological University, Singapore. His research interests include development and validation of noninvasive optical diagnostic tools.